Droplet clustering signatures of entrainment in clouds

Suryadev Pratap Singh [*]
Department of Physics, Michigan Technological University, Houghton, Michigan 49931, USA

Michael L. Larsen [†]
Department of Physics and Astronomy, College of Charleston, Charleston, South Carolina 29424, USA;
Laboratory for Fluid Physics, Pattern Formation and Biocomplexity,
Max Planck Institute for Dynamics and Self-Organization, Göttingen 37077, Germany;
and Department of Physics, Michigan Technological University Houghton, Michigan 49931, USA

Jesse C. Anderson, Hamed Fahandezh Sadi, Jae Min Yeom, Will Cantrell, and Raymond A. Shaw [‡]
Department of Physics, Michigan Technological University, Houghton, Michigan 49931, USA

(Received 6 March 2026; accepted 18 August 2026; published 15 September 2026)

The spatial distribution of cloud droplets is relevant for various microphysical processes, such as condensational growth, collision coalescence, riming and aggregation, and radiative transfer. Cloud droplets and other hydrometeors exhibit clustering at dissipation scales and above due to turbulence-induced preferential concentration. Here, we investigate the role of entrainment in modulating the scale-dependent clustering of cloud droplets and explore how this mechanism differs from inertial clustering. We have performed experiments in the Pi convection-cloud chamber, and imaged 2D droplet fields in the cloud-top region where dry-air entrained through an open cylindrical flange leads to an entrainment-mixing process. Captured images are processed to retrieve instantaneous two-dimensional velocity fields using particle image velocimetry, scale-dependent clustering is explored using the radial distribution function, and spatial nonuniformity is quantitatively identified through the Kolmogorov-Smirnov test. The analysis reveals that the observed droplet clustering is scale dependent and occurs intermittently with enhanced magnitude in the region influenced by entrainment. Furthermore, the strength of clustering and spatial nonuniformity increases with mean entrainment flow. Using a novel bias-mitigation method, we estimate that the strength of clustering (pair-correlation function) roughly doubles in the presence of entrainment (downdraft), compared to no-entrainment (updraft) regimes. Such an entrainment-clustering relationship could be used to help identify and decipher the role of entrainment in modulating localized clustering in natural atmospheric clouds.

DOI: 10.1103/4hrw-nf7t

I. INTRODUCTION

Spatial clustering of particles in turbulent flows is ubiquitous in various natural and industrial processes, such as planetesimal formation [1], organization of nonmotile phytoplankton [2,3], mixing of fuel particles in the turbulent combustion flows [4,5], and among aerosols and clouds in the Earth's atmosphere [6–8]. Cloud droplets in a clustered community can experience enhanced competition for water vapor and undergo slowed growth, while a droplet sufficiently far from its competing neighbors can grow faster, impacting the overall size distribution [9,10]. For a falling collector droplet, the efficiency of collision coalescence can change if ambient cloud droplets are clustered along the intercepted path [7]. Depending on how the cloud droplets are distributed in space, radiative transfer can deviate from the expected exponential extinction (given by Beer-Lambert law), altering the localized radiative heating or cooling profile [11–14].

Spatial distribution of droplets depends on their mechanical transport by turbulent structures and thermodynamic responses to scalar fields, potentially modulated by entrainment and scalar mixing [6,15–18]. Entrainment is the macroscopic ingestion of ambient fluid into a turbulent stream, such as an ejector nozzle vacuuming in surrounding air, or a rising cloud updraft capturing dry environmental air, whereas scalar mixing is the subsequent microscopic blending of that fluid down to the molecular level, such as utilizing vortical structures and thermal conduction to eliminate temperature streaks in a combustor, or turbulent stirring and molecular diffusion to evaporate cloud droplets [19,20]. Entrainment creates sharp, localized scalar mixing zones [17,21], introducing localized fluctuations in scalar fields that can reshape the cluster structures independent of particle

*Contact author: ssingh45@mtu.edu
†Present address: Department of Physics and Astronomy, College of Charleston, Charleston, South Carolina 29424, USA.
‡Contact author: rashaw@mtu.edu

Published by the American Physical Society under the terms of the Creative Commons Attribution 4.0 International license. Further distribution of this work must maintain attribution to the author(s) and the published article's title, journal citation, and DOI.

inertia [22]. Additionally, particles centrifuge away from regions of high vorticity and accumulate in high-strain zones based on their Stokes number, developing spatial clustering [6,23,24].

It is widely established that cloud droplets exhibit preferential clustering at dissipation scales, a behavior that can be attributed to turbulence-induced preferential concentration [6,8,18,25–28]. Clustering has also been reported at inertial-subrange scales; however, the small Stokes numbers of atmospheric cloud droplets indicate that droplet inertia alone is unlikely to account for such behavior [18,29,30]. Instead, entrainment-mixing processes between cloudy and clear air can be expected to play an important role in shaping scale-dependent clustering and spatial nonuniformity at inertial-subrange scales [8,18]. Similar effects have been reported in laboratory wind-tunnel studies, where larger-scale clustering appears due to the scalar mixing of the droplet field, whereas smaller-scale clustering depends on droplet Stokes numbers [16,28,31]. The primary objective of this work is to examine the potential role of entrainment in modulating cloud-droplet clustering. Here, clustering indicates any departure from perfect randomness, given by the radial distribution function [8,32–34]. Moreover, since entrainment inherently occurs near cloud boundaries where thermodynamic and microphysical properties are intrinsically inhomogeneous and nonuniform, we also address how such spatial nonuniformities can be identified and properly accounted for when quantifying spatial clustering using a novel bias-mitigation method.

Many field experiments indicate that entrainment-mixing can modulate scale-dependent clustering [18,34–37]. In particular, Thiede *et al.* [34] reported that stronger clustering occurs intermittently, challenging our understanding of small-scale microphysical processes. However, these observed clustering enhancement zones have not been studied in detail due to difficulties in setting up collocated high-resolution measurements of entrainment and clustering from rapidly moving instruments in airborne field experiments. Such experiments can more easily be set up in a controlled cloud chamber and studied under known initial and boundary conditions. Hence, to investigate the role of entrainment in modulating clustering, we have conducted experiments in the Pi convection cloud chamber [38].

The radial distribution function (RDF), $g(r)$, and the pair-correlation function ($\mathrm{PCF}(r) \equiv g(r) - 1$) have been widely used to characterize scale-dependent spatial clustering in turbulent flows, which is defined as the ratio of the observed density of particle pairs separated by scale r to the expected density if they follow a Poisson distribution [8,33,34,39]. For a planar density, it is computed by Eq. (1)

$$g(r) = \sum_{i=1}^{N} \frac{\psi_i(r)}{N(N-1)\delta A/A}, \tag{1}$$

where N is the total droplet count in a plane of area A and $\psi_i(r)$ is the total number of particles located at radial distance r from a given particle within annular area δA in the same plane [33]. If $g(r)$ exceeds 1, more particle pairs are separated by r than would be expected in a Poisson distribution, and particles are found to be clustered at that scale. We have used $g(r)$ to estimate scale-dependent clustering, while a concurrent and collocated instantaneous velocity field, retrieved using particle image velocimetry (PIV) analysis, has been used to decipher the role of entrainment on clustering.

One of the primary assumptions in the estimation of the RDF is that droplets are homogeneously distributed in space [33]. However, this assumption is usually not valid in experiments due to instrumental biases, boundary conditions, and inherent microphysical processes such as sedimentation and entrainment [21]. These biases can introduce a varying degree of uncertainty in RDF calculation and interpretation [18,40]. To estimate spatial nonuniformity in droplet fields, we have employed a nonparametric Kolmogorov-Smirnov (K-S) test, which compares the cumulative distribution of observed droplet positions with that of a reference distribution [18]. Further, a novel bias-mitigation method has been developed to mitigate the effect of nonuniformity on the RDF so that the relative role of entrainment on scale-dependent clustering can be accurately estimated.

Details of the conducted experiments, methodology, and statistical tools employed to analyze the recorded datasets are described in Sec. II. Characteristics of the droplet clustering, nonuniformity, and their link to entrainment is presented in Sec. III. We have estimated the relative role of entrainment on clustering in the same section. Furthermore, we discuss the implications of entrainment-induced enhanced clustering for atmospheric clouds and precipitation with concluding remarks in Sec. IV.

II. EXPERIMENTAL DETAILS AND METHODOLOGY

A. Experimental details

We investigate the entrainment-mixing process in a cloudy turbulent convection flow by steadily injecting clear and dry air into a cloud-filled chamber and examine to see how entrainment influences the spatial distribution of cloud droplets at different scales [Fig. 1(a)]. The experiment has been conducted for two different convective turbulence levels, corresponding to temperature differences of $\Delta T = 9$ and 18 K, and for two different aerosol injection rates ($\dot{n} = 0.5$ and $1\,\mathrm{cm^{-3}\,s^{-1}}$) to create base clouds [Fig. 1(b)]. Further, we quantify the clustering using two analysis methods: We use the RDF to look at the scale dependence of clustering, and we use the K-S test to look at the spatial nonuniformity of the droplet concentration field.

Experiments have been carried out in the Pi convection-cloud chamber, containing a cylindrical volume of $3.14\,\mathrm{m^3}$, 2 m diameter, and 1 m height. To develop clouds in the chamber, supersaturation is generated through turbulent moist Rayleigh-Bénard convection by maintaining the top panel at a lower temperature compared to the bottom one. To ensure a continuous moisture supply and maintain supersaturation, the bottom panel contains a water reservoir, while the remaining surfaces are kept wet using moist filter paper. More details about the Pi chamber have been introduced in Ref. [38]. When hygroscopic aerosol particles are injected into supersaturated conditions, clouds develop.

For both the turbulence levels (having $\Delta T = 9$ and 18 K), the temperature of the bottom and top panels can be calculated

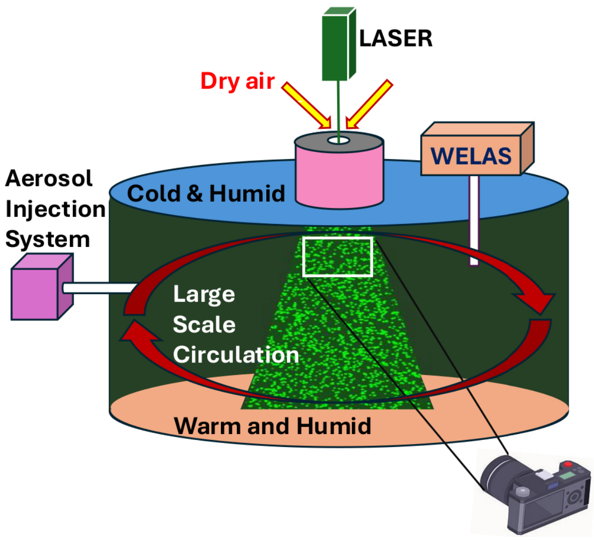

(a)

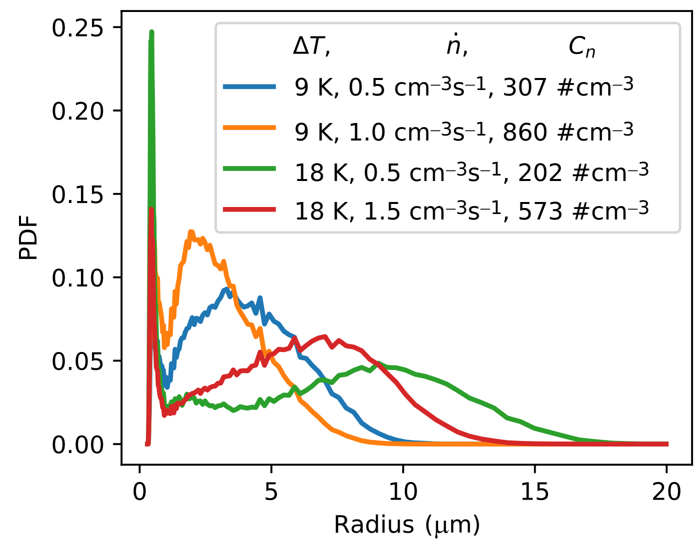

(b)

FIG. 1. (a) Schematic of experimental setup. (b) Probability density functions (PDFs) of the cloud-droplet radius derived from Welas measurements for the four experimental conditions. "#" represents the droplet count.

using $T_b = T_m + \Delta T/2$ and $T_t = T_m - \Delta T/2$, respectively, whereas mean temperature (T_m), which is the temperature of the cylinder side walls and the bulk cloud [30], has been maintained at $T_m = 293.15$ K. For cloud condensation nuclei (CCN), precise concentrations of hygroscopic sodium chloride (NaCl) particles having a mean mobility diameter of 130 nm, mixed with $2\,\mathrm{L\,min^{-1}}$ flow of dry air, have been injected in the chamber, providing two different injection rates of $\dot{n} = 0.5$ and $1\,\mathrm{cm^{-3}\,s^{-1}}$ for each of the two temperature gradients. Details about the aerosol injection system, including aerosol generation, size selection, and concentration control, have been described in Ref. [41].

We start each experiment with steady-state convection with negligible CCN/cloud droplets in the chamber to minimize any residual effects. Next, CCN are injected continuously to generate clouds, which roughly takes 30 min to reach thermodynamic-microphysical steady state. Then, the number concentration and size distribution of clouds are measured using an optical counter, Palas Welas-2000, for 20 min at a measurement frequency of 1 Hz.

During measurements, the Welas instrument continuously samples cloudy air at $5\,\mathrm{L\,min^{-1}}$ from the chamber, whereas the aerosol injection system adds $2\,\mathrm{L\,min^{-1}}$ of dry air into it, resulting in a flow imbalance of $3\,\mathrm{L\,min^{-1}}$ within the chamber. To maintain isobaric conditions, in these experiments the chamber naturally develops an inflow of $3\,\mathrm{L\,min^{-1}}$ through an open cylindrical flange, located in the center of the top panel, which leads to an entrainment-mixing process beneath the flange (hereafter referred to as the entrainment zone). Entrained flow through the same flange has also been utilized in various earlier studies, e.g., studying the microphysical responses of entrainment to clouds and studying the vertical profile of laboratory-generated clouds using a centimeter-scale resolution lidar [21,41,42].

A vertical sheet of laser light, generated using a continuous green laser and Powell lens of 30° fan angle, passes through the same flange and illuminates cloud droplets, whereas a digital camera (Sony-α7 III), mounted on the lateral wall, captures high-resolution images at 60 frames/s through the ITO-coated optical window [Fig. 1(a)]. To prevent condensation on the optical window, we have used ITO-coated (indium tin oxide, an electrically conductive thin film) glass [43], heated slightly above the dew point at the location of the window, maintaining high optical transparency (85%–90%) and enabling high-resolution imaging of cloud droplets without disturbing the flow.

Due to the diverging intensity of the laser sheet and the limited focus area of the camera, a region of 16 cm × 8.5 cm having reasonably uniform intensity and focus in the entrainment zone has been selected for all image-based analysis. The analyzed region is located 5 cm below the cloud-top boundary (entrainment interface). Consequently, these measurements primarily reflect cloud-edge and entrainment-mixing processes rather than conditions within the cloud core. Despite this mostly uniform intensity and focus, this region of interest within each image can still contain systematic biases that have been mitigated using different statistical techniques described below. All images are calibrated (pixel resolution of 130 μm) and preprocessed (grayscale conversion, contrast stretching, background removal, and thresholding) to derive two-dimensional droplet location fields. Furthermore, we apply the find-contours and minimum enclosing circles method [44] to track the position of droplets, enabling further processing and retrieval of instantaneous two-dimensional velocity fields, spatial nonuniformity, and scale-dependent clustering.

B. PIV method

We have used openPIV, a computational tool for PIV, to extract instantaneous two-dimensional velocity fields from all the processed images [45]. In this method, an FFT-based (fast Fourier transform) window deformation algorithm in three passes having interrogation areas (in pixels) of 256 × 256,

128×128, and 64×64 with window overlap of 50% have been used, which yields 2D velocity fields with a spatial resolution of 4.16 mm and a temporal resolution of 16.66 ms.

Although PIV analysis often involves the use of extra tracer particles, we have avoided this sort of seeding in this study because such tracers, being in the micrometer-size range, can alter the cloud-microphysical interactions and can also contaminate tracking of cloud droplets for the clustering analysis. Cloud droplets themselves behave like reasonable fluid tracers, because the Stokes number for the size distribution of the cloud droplets in the chamber [Fig. 1(b)] lies in the range of 10^{-5} to 10^{-3} [30].

Uncertainty in the derived velocity vectors can come from various sources such as measurement bias, sedimentation, inherent clustering, and the entrainment-mixing process. If the velocity vectors are not robust based on a minimum signal-to-noise ratio [defined as the ratio of the highest peak intensity to second-highest peak in the three-dimensional (3D) correlation map of pixel displacements] of 1.3, they have been rejected. The algorithm used also rejects noisy velocity vectors, which occur mostly when the flow is predominantly perpendicular to the laser plane (which occasionally happens due to the inherent turbulent characteristics of the flow). Note that instantaneous entrainment and updraft scenes have been identified based on image-mean vertical velocity; hence, to avoid miscategorization, if the velocity field at any time contains less than 20% valid vectors, the full velocity field at that instant was rejected. In this way, we rejected 30%–40% of the image dataset.

C. Statistical tools and uncertainty

We use the RDF to quantify the scale-dependent clustering of cloud droplets; however, RDF estimates are subject to uncertainties arising from pixelation errors, edge effects, and spatial nonuniformity, which must be accounted for. Pixelation errors originate from the finite spatial resolution of the imaging system, leading to a positional uncertainty of ± 0.5 pixels in droplet locations within the image plane. To account for this uncertainty, droplet positions are randomly jittered within ± 0.5 pixels of their observed locations, and the RDF is recomputed for 50 such realizations [8,34]. The median RDF over these realizations is used for all subsequent analyses.

Uncertainties due to edge effects occur due to the unavailability of all possible particle pairs for a particle located near the edge of the image [33] (some locations a distance r away from a given particle lie outside the image boundary, and—for a real system like this—periodic boundary conditions often used for these sorts of computations in modeling studies would not be appropriate). There are many methods to adjust for these effects; e.g., the guard-area approach is commonly used for experimental datasets [33]. However, the guard-area approach can profoundly limit the clustering information from a dataset due to the reduced number of available particle pairs. To optimally utilize all detected droplet pairs, another method, called the normalization-on-the-fly method, has been employed [34]. In this method, if particle pairs for a particle located near the edge are only available in a fraction of the annular area, only that fraction of the area is considered to calculate the droplet density. This method accurately estimates clustering close to the scale of the image dimension, provided the number of particle pairs is sufficiently large [34].

Systematic spatial nonuniformity in observed droplet fields may arise from nonuniformity in the camera focus, the diverging nature of the laser sheet, and its finite thickness (which, in this system, is estimated to be 100s of micrometers); these nonuniformities introduce systematic biases in the RDF estimation. The combined effect of these biases has been estimated using a "superimage" method, which is similar to the superhologram method employed in 3D holographic datasets [8,34]. As adapted to this study, we generate a "superimage" that contains positions of all droplets from a collection of 3600 images and randomly shuffle their positions within ± 0.5 pixels 100 times for statistical robustness. Further, from the superimage, we reconstruct a sequence of images with the same number of droplets per image by sampling from the superimage (without replacement). In this way, we intentionally remove image-by-image localized clustering information (if it is there), but preserve the systematic biases related to nonuniform particle detection efficiencies throughout the image domain. We calculate an RDF using all these shuffled and randomly permuted images and average them to get an underlying systematic bias in RDF [$g_s(r)$]. After its computation, $g_s(r)$ is subtracted from the total measured RDF [$g_t(r)$] of each image to obtain a "bias-corrected estimated RDF" [$g_c(r)$] as follows:

$$g_c(r) = 1 + g_t(r) - g_s(r). \tag{2}$$

$g_c(r)$ has departures from unity that are plausibly primarily due to the dynamical and microphysical properties of the cloudy system, rather than due to the combination of measurement biases and true microphysical conditions. To reduce uncertainty resulting from the limited number of particle pairs per image, all correlation analysis that follows has been performed on a 0.5-s running average (over 30 samples) dataset for statistical robustness.

The estimated RDF using the superimage or superhologram method has been used to decide whether the total RDF contains a meaningful signal or not [8,34]. However, this technique's adequacy in fully quantifying uncertainty or systematic bias remains to be established. Further, when we subtract the superimage-based RDF from the total one, it is not clear if all the systematic bias has been accounted for.

To address this, we have tested the accuracy of the superimage method on a simulated 2D Matérn process, which has a closed-form expression for RDF in different dimensions and can be easily simulated for spatially uniform, but clustered fields [33,46]. After modifying the simulated system with artificial systematic biases, we observe that the superimage method indeed reduces the effect of some—but not all—of the added systematic bias. Further, we find that the RDF needs to be adjusted for the image-specific droplet counts relative to the background number to improve the mitigation of the systematic bias. This "background number" represents a measure of the drop counts that would be present if there is no spatial nonuniformity and no systematic bias. Unfortunately, this true drop count number is not known in real experimental conditions. However, we can get a quantitative measure of how the scale dependence of clustering differs between two conditional samples having the same background (i.e., same experimental conditions). Details of this method can be found in Appendix A.

For this work, it is important to note that the cloud droplet field can be inhomogeneous (spatially nonuniform) due to inherent microphysical processes, including entrainment and mixing, apart from systematic instrumental bias. We have used a nonparametric, K-S test to identify such nonuniformity during entrainment and updraft [18,47]. All images for a particular set of boundary conditions (ΔT and $\dot{n}$) are classified into two classes based on whether their image-mean vertical velocity is downward (entrainment) or upward (no entrainment). Furthermore, images from each class are horizontally split into two parts (top and bottom) in such a way that the average counts of droplets over all images of that class in both partitions are forced to be approximately equal. (Note that the shift in partitioning from the midpoint of the image is less than 6% of the vertical size of the image, suggesting that partitions are only marginally nonuniform.) In this way, we avoid the systematic instrument bias and, as a result, any estimated transient vertical nonuniformity can be attributed to microphysical and dynamical processes.

In a truly uncorrelated system, the expected difference in drop number between the "top" and "bottom" of the image would be 0, with a distribution governed by the Skellam distribution [48]. Based on the properties of the distribution—and following the approach introduced in Ref. [18]—we define a parameter, δ_y

$$\delta_y = \frac{N_A - N_B}{\sqrt{\frac{N_A+N_B}{2}}}, \tag{3}$$

where N_A and N_B represent droplet counts in the top and bottom partitions, respectively. δ_y is calculated for both the conditions ($w < 0\,\mathrm{m\,s^{-1}}$ and $w > 0\,\mathrm{m\ s^{-1}}$). Furthermore, in each case, 1000 Monte Carlo (MC) simulations have been performed to calculate the mean $\delta_{y,\mathrm{mc}}$ to estimate natural variability in the droplet counts, assuming that mean droplet counts in the top and bottom partitions follow a binomial (perfectly random) distribution. To estimate nonuniformity with respect to their natural variability, the cumulative distribution function (CDF) of the observed $\delta_{y,o}$ is compared to that of $\delta_{y,mc}$, where the maximum absolute difference between the CDFs is denoted as the K-S distance (h_y). To establish that the variability is significant, h_y is calculated for each realization of the MC simulations, as well as the δ_y with respect to the mean $\delta_{y,mc}$. A PDF of $h_{y,mc}$ is compared to h_y at different significance levels to assess whether nonuniformity is robust and above the inherent variability.

III. RESULTS

The experiments performed using two temperature differences (ΔT) and two aerosol injection rates ($\dot{n}$) span four distinct microphysical regimes, which enables us to investigate the entrainment-clustering relationship in varying microphysical and thermal conditions. The PDFs of cloud-droplet size distributions along with the droplet concentration (C_n), in steady state (averaged over 20 min), are shown in Fig. 1(b). The case with $\Delta T = 18\,\mathrm{K}$ and $\dot{n} = 0.5\,\mathrm{cm^{-3}\,s^{-1}}$ represent clean clouds, characterized by a modal radius of approximately 10 µm and a C_n of 202 $\mathrm{cm^{-3}}$, whereas $\Delta T = 9\,\mathrm{K}$ and $\dot{n} = 1.0\,\mathrm{cm^{-3}\,s^{-1}}$ correspond to polluted-clouds with a modal radius of approximately 2 µm and a C_n of 860 $\mathrm{cm^{-3}}$ [49]. The remaining two cases represent moderately polluted conditions between these two extremes while having distinct thermal forcings.

A. Flow characteristics and entrainment

The Pi chamber sets up Rayleigh-Bénard convection under the specified temperature gradients, characterized by Rayleigh Number Ra $\approx 10^9$, and Prandtl Number Pr ≈ 0.7, resulting in a robust large-scale circulation [50–52]. For the present set of experiments, large-scale circulation consisting of single roll [Fig. 1(a)], having mean horizontal velocities of 11 and 17 cm/s are observed in the entrainment zone for the temperature differences of 9 and 18 K, respectively, which is consistent with the previously reported circulation strengths [52].

Turbulence characteristics derived from PIV-retrieved velocity fields yield a kinetic energy dissipation rate ε of order $10^{-4}\,\mathrm{m^2\,s^{-3}}$ and a Kolmogorov length scale ($\eta = (\frac{\nu^3}{\varepsilon})^{1/4}$) of order 1 mm [30,53]. Here, to estimate turbulent quantities using 2D velocity fields, we assume that flows are incompressible, locally isotropic and locally homogeneous [54]. A detailed derivation of ε for 2D velocity fields is presented in Appendix B. Further, due to coarse spatial resolution of the velocity field, compared to the Kolmogorov scale and unavailability of third dimension in the measured velocity field, uncertainty in estimated dissipation rate can be up to $\pm 40\%$. It can propagate 10% uncertainty in η and 20% in Stokes number [55]. Hence, ε and η are presented with order of magnitude precision only. Furthermore, the Stokes numbers (St) for the clean ($\Delta T = 18$ K and $\dot{n} = 0.5\,\mathrm{cm^{-3}\ s^{-1}}$) and polluted ($\Delta T = 9$ K and $\dot{n} = 1.0\,\mathrm{cm^{-3}\ s^{-1}}$) cloud cases are 4×10^{-3} and 5×10^{-4}, respectively, while the remaining cases fall between these two values. Due to the turbulent structure of the flow, the local instantaneous flow can be in any direction; hence, we have determined updrafts or downdrafts based on the image-mean vertical velocity, where downdraft ($w < 0\,\mathrm{m\ s^{-1}}$) represents entrainment as it is associated with a decrease in droplet counts (N) (Table I).

Episodic plumes that rise from the heated bottom plate and the flow through the open cylindrical flange downward from the top of the chamber lead to alternating episodes of entrainment-induced downward motion ($w < 0$) and updraft-driven upward motion ($w > 0$) within the entrainment zone. Because these two flow regimes originate from distinct thermodynamic and dynamical conditions, they are expected to drive different cloud microphysical environments, including variations in droplet number concentration, size distribution, and scale-dependent clustering. In the present experiments, the droplet size distribution cannot be reliably inferred directly from the PIV measurements due to limited pixel resolution. However, the relative positions of droplets can be tracked accurately, enabling robust estimation of velocity vectors and the RDF. All droplet counts reported hereafter are based on the number of tracked droplets per image. A linear correlation analysis between droplet count and vertical velocity shows that entrainment leads to a decrease in

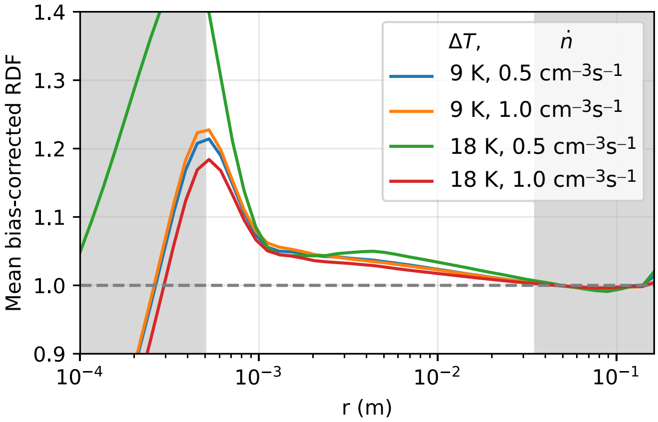

FIG. 2. 10-min mean bias-corrected RDF [$\overline{g_c(r)}$] for all four experimental conditions. Scales with limited accuracy are shaded in gray.

droplet counts (Table I), which is consistent with localized inhomogeneous mixing reported by Yeom *et al.* [42] (see also Appendix C).

B. Stronger clustering appears intermittently

For each experimental condition, bias-corrected RDFs are calculated using Eq. (2), which has been averaged over 10 min to get the mean clustering strength at different scales (Fig. 2). Scales that do not contain robust information have been shaded in gray. Limitations on the lower scales are attributed to laser-sheet thickness and finite-resolution uncertainties, whereas limitations on the upper scales partially arise due to edge effects. However, we have considered the upper limit more conservatively in subsequent analysis, where such a limit avoids spurious noise due to division. Note that $g_s(r)$ may not account for all systematic bias [8,34], which we further test and refine in Sec. III C.

Figure 2 shows scale-dependent clustering of cloud droplets where the strongest clustering is observed near the Kolmogorov scale, and its strength decreases with increasing scale, eventually vanishing at the scale of ~3 cm. Similar clustering strengths and qualitative scale-dependent structure have been reported from field studies [8,34]. However, discrepancies can be observed because a confined, thermally driven laboratory flow differs from an unconfined, dynamically forced atmosphere. Further, the sharp increase in RDF trend below 1 mm likely indicates clustering due to mutual hydrodynamic interaction between droplets, consistent with observations by Yavuz *et al.* [56]. Since we do not observe significant differences in clustering-behavior among the four different experimental conditions, we will only present results corresponding to the two extremes: clean, strongly forced clouds ($\Delta T = 18\,\mathrm{K}$, $\dot{n} = 0.5\,\mathrm{cm^{-3}\,s^{-1}}$) and polluted, weakly forced clouds ($\Delta T = 9\,\mathrm{K}$, $\dot{n} = 1.0\,\mathrm{cm^{-3}\,s^{-1}}$) in the analysis that follows. (Analysis of the other cases produced similar results).

Figure 3 shows a time series of the 0.5-s (30-image) running mean of the bias-corrected RDF at two scales, $r = 0.001$ m and $r = 0.01$ m, for clean and polluted clouds over a temporal interval lasting of 100 s (for clarity in seeing the fluctuations). $r = 0.001$ m represents the Kolmogorov length scale for the flows in our experiments, and $r = 0.01$ m is approximately where the dissipation range transitions to the inertial subrange. Although $g_c(r)$ shows strong temporal variability at both the scales, $g_c(r = 0.01\ \mathrm{m})$ is usually weaker than $g_c(r = 0.001\ \mathrm{m})$. Further, clustering at both scales is strongly correlated (Pearson correlation coefficient, $r > 0.9$, $p = 0.0$), indicating that clustering at different scales is

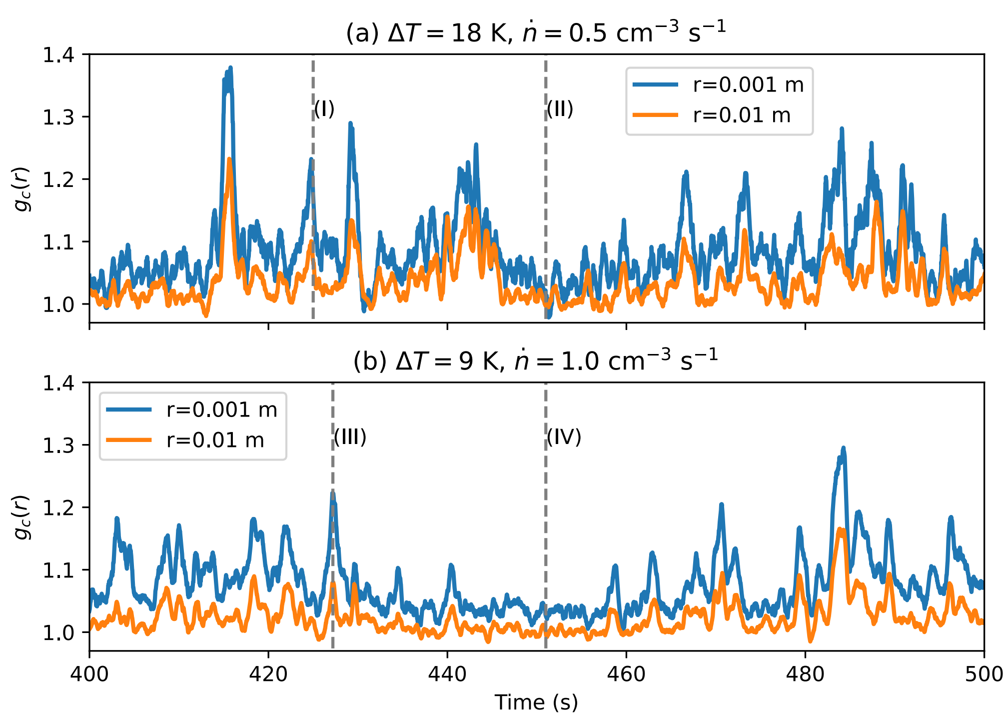

FIG. 3. Time series of $g_c(r)$ at $r = 0.001$ and 0.01 m for (a) clean, strongly forced clouds and (b) polluted, weakly forced clouds. Four snapshots of droplet fields, corresponding to weak and strong clustering (marked as I–IV) for both the cases are shown in Fig. 4.

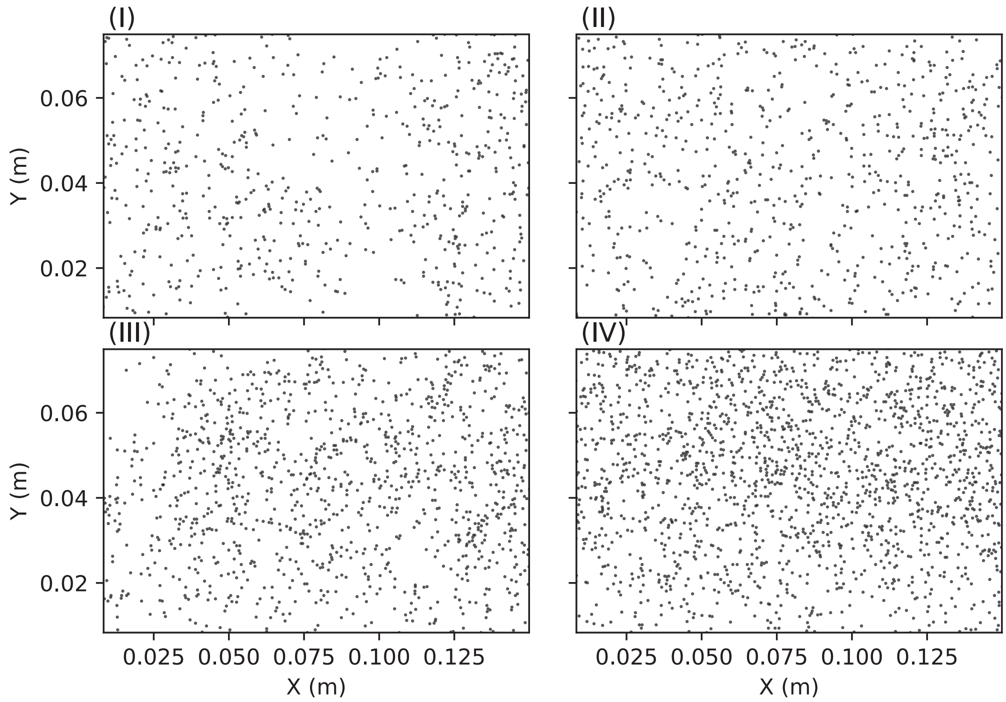

FIG. 4. 2D snapshots of cloud-droplet fields under different clustering conditions. (I) Strong and (II) weak clustering in clean clouds ($\Delta T = 18$ K, $\dot{n} = 0.5$ cm^{-3} s^{-1}); (III) strong and (IV) weak clustering in polluted clouds ($\Delta T = 9$ K, $\dot{n} = 1.0$ cm^{-3} s^{-1}) (see Fig. 3).

coupled. In both clean and polluted conditions, $g_c(r)$ surges intermittently at both scales, which is consistent with reported field observations [34]. Snapshots of cloud-droplet fields under different clustering conditions for clean and polluted clouds (marked as I, II, III, and IV in Fig. 3) are shown in Fig. 4 (for other cases, see Appendix D).

It has been suggested that cloud-top entrainment can potentially modulate the strength of clustering and further microphysical responses [35,37]. To investigate such behavior, we calculate the correlation coefficient between $g_c(r = 1$ mm), horizontal and vertical velocity (u, w), 2D rms speed ($v_{\rm rms}$), and per-image droplet counts (N), as shown in Table I (see Appendix E for scatter plot). Note that all correlations have been performed on a 0.5-s running mean dataset after removing all invalid velocity vectors and corresponding RDFs. The uncertainty in the resulting correlation coefficients, estimated using the Fisher z transform, is less than 0.03 at the 95% confidence level for all cases.

The linear correlation analysis between different variables indicates that u is poorly correlated with $g(r)$ at $r = 0.001$ m– (Note that the direction of the large-scale circulation flips when we change thermal boundary conditions from $\Delta T = 9$ to 18 K.) $v_{\rm rms}$ and $g_c(r = 1$ mm) are also poorly correlated. The strongest correlations with $g_c(r = 1$ mm) are with vertical velocity, which is moderately anticorrelated, and N, which is strongly anticorrelated. A moderate correlation between N and w also exists. These results help reinforce the expected behavior that downdrafts tend to be associated with entrainment events, in which the otherwise relatively uniform droplet concentration is reduced. Therefore, we speculate that clustering increases with entrainment.

Based on the above correlation analysis, entrainment-induced mixing can be a factor in enhancing clustering. However, the clustering estimation might be influenced by enhanced spatial nonuniformity over the sample volume during entrainment events. We therefore seek a method to estimate and account for nonuniformity and the change in droplet counts that occur during entrainment in the estimation of the RDF. Using this method, we can more robustly quantify the relative role of entrainment in the observed clustering.

C. Relative estimation of entrainment effect on clustering

Using the methodology for the KS test described in Sec. II, the CDF of δ_y and the PDF of the KS distance, h_y, for clean

TABLE I. Pearson correlation (uncertainty <0.03) among different variables: horizontal (u) and vertical velocity (w), root-mean-squared velocity ($v_{\rm rms}$), droplet counts per image (N), and $g_c(r = 1$ mm).

$\Delta T, \dot{n}$ →	9 K, 0.5 cm^{-3} s^{-1}	9 K, 1.0 cm^{-3} s^{-1}	18 K, 0.5 cm^{-3} s^{-1}	18 K, 1.0 cm^{-3} s^{-1}
w and N	0.53	0.40	0.67	0.60
u and $g_c(r)$	0.28	0.48	−0.03	−0.21
w and $g_c(r)$	−0.41	−0.39	−0.52	−0.55
$v_{\rm rms}$ and $g_c(r)$	0.11	0.35	−0.11	0.25
N and $g_c(r)$	−0.68	−0.79	−0.71	−0.88

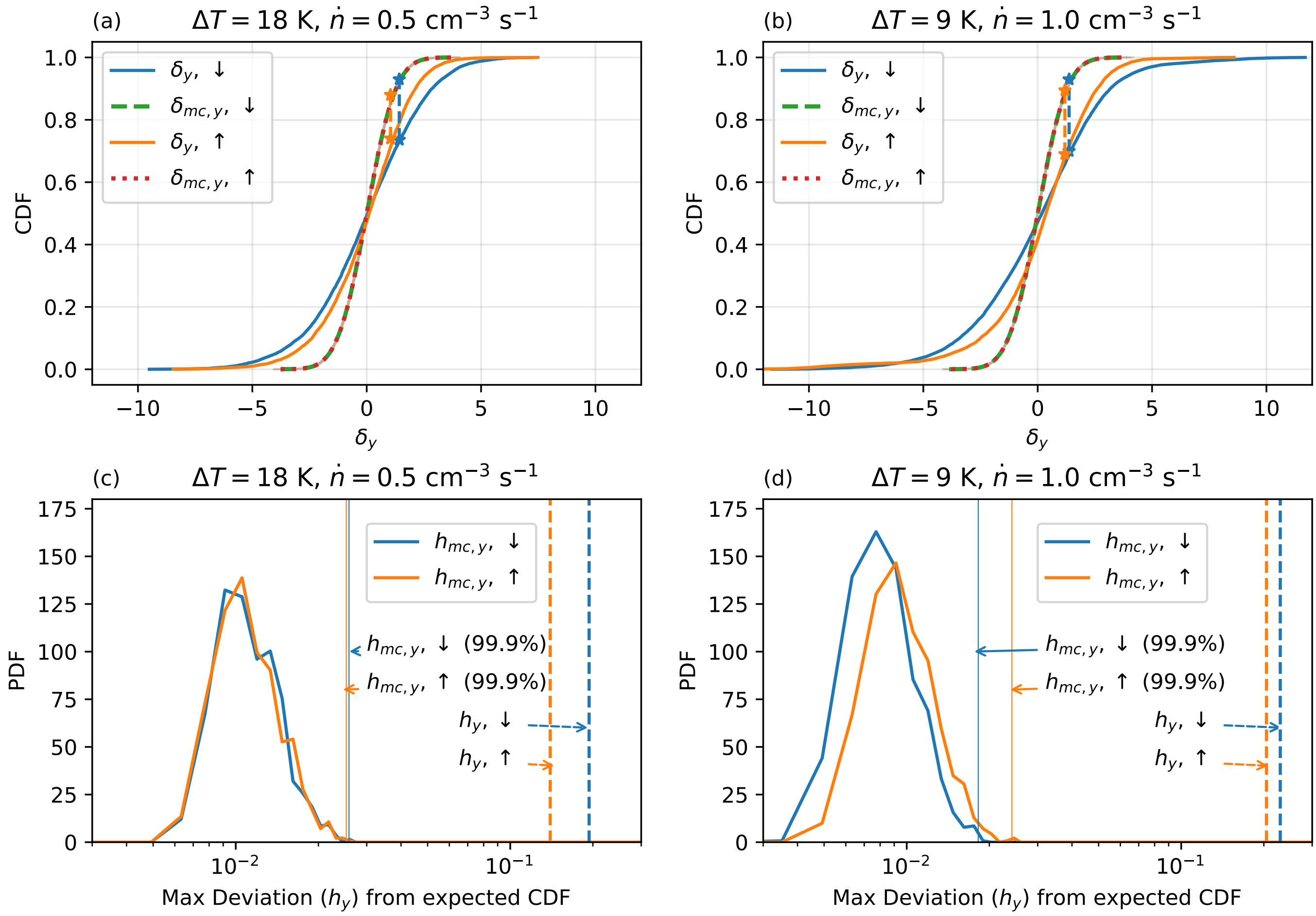

FIG. 5. (a), (b) CDFs of the δ_y for 1000 MC simulation and observed counts, where δ_y is the normalized difference in counts between the top and bottom portions of the PIV sample region. Vertical dashed blue and orange lines represent KS distance (h_y) for downdraft and updraft. (c), (d) PDFs of the KS distance h_y for updraft and downdraft (entrainment) conditions from 1000 MC simulations with respect to their mean CDFs. Solid vertical lines show empirical uncertainty at 99.9% bound, whereas dashed vertical lines correspond to measured droplet fields.

and polluted conditions are shown in Fig. 5. Larger values of the KS distance (h) correspond to stronger evidence for inhomogeneity. The CDF of $\delta_{mc,y}$, $\downarrow$, representing entrainment, and $\delta_{mc,y}$, $\uparrow$, representing updraft, largely overlap, which indicates that both cases exhibit similar natural variability. In contrast, comparison of δ_y with $\delta_{mc,y}$ shows that the scale and intensity of the observed nonuniformity exceed the natural variability expected for perfect randomness [Figs. 5(a) and 5(b)]. The maximum deviation of the observed CDF from the expected distribution of δ_y quantifies the relative certainty of the nonuniformity. Figs. 5 (c) and 5(d) shows that the observed droplet fields for both entrainment and updraft are vertically nonuniform at a >99.9% significance level. A comparable level of nonuniformity has also been reported in atmospheric clouds using holographic observations [18]. Moreover, the distribution of h_y indicates that entrainment exhibits even stronger evidence for nonuniformity than the updraft case for both clean and polluted clouds.

The stronger nonuniformity associated with entrainment, compared to the updraft case, can potentially introduce uncertainty when comparing scale-dependent clustering between the two flow regimes. Although the superimage method is intended to remove systematic bias, its effectiveness in reducing bias has not been evaluated for situations in which the droplet field exhibits systematic variations in both spatial distribution and concentration, as is likely in the present observations, where entrainment can be active or absent. To address this limitation, we develop a bias-mitigation method that enables accurate estimation of relative strength in clustering when updraft and downdraft conditions are characterized by different levels of nonuniformity.

As described in Appendix A, Eq. (4) has been used to estimate relative clustering strength at different scales during entrainment (downdraft) compared to no-entrainment (updraft) conditions:

$$\frac{\mathrm{PCF}_{\downarrow}(r)}{\mathrm{PCF}_{\uparrow}(r)} = \frac{g_{c,\downarrow}(r) - 1}{g_{c,\uparrow}(r) - 1} = \frac{N_{\downarrow}[g_{\downarrow,t}(r) - g_{\downarrow,s}(r)]}{N_{\uparrow}[g_{\uparrow,t}(r) - g_{\uparrow,s}(r)]}, \tag{4}$$

where $\uparrow$ represents updraft and $\downarrow$ denotes downdraft, which is associated with entrainment. Figure 6 shows the relative strength of clustering as a function of spatial scale for clean and polluted clouds, calculated using the bias-mitigation method. The standard deviation represents sample-to-sample variability, while the standard error quantifies the uncertainty in estimating the mean relative clustering. Details of the error analysis are also provided in Appendix F. A ratio of unity in

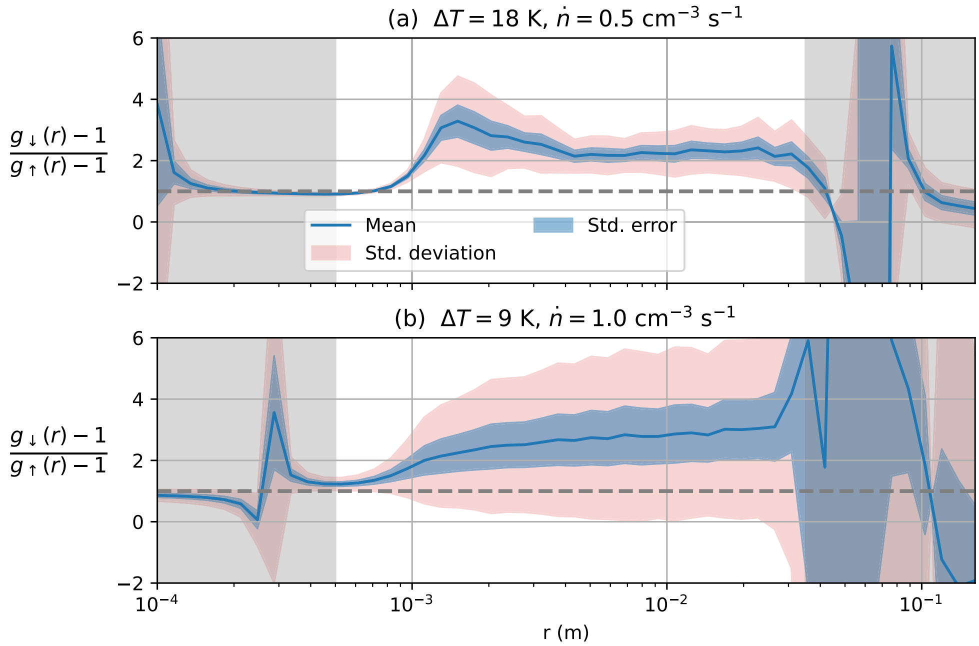

FIG. 6. Relative strength of scale-dependent clustering due to entrainment (downdraft) and no entrainment (updraft) for (a) clean, strongly-forced clouds and (b) polluted, weakly forced clouds. Blue shading represents standard error, whereas red shading corresponds to standard deviation.

Eq. (4) indicates that updraft and entrainment exhibit the same level of clustering. Despite substantial sample-to-sample variability, the analysis shows that entrainment generally exhibits stronger clustering than in updraft over scales greater than the Kolmogorov scale.

Below the Kolmogorov scale, turbulence-induced preferential concentration dominates regardless of whether entrainment is present. Consequently, the effect of entrainment on relative clustering is marginal at these sub-Kolmogorov scales. In contrast, within the resolved portion of the inertial subrange, the impact of entrainment on clustering is pronounced, with relative clustering enhancing by a factor of 2–3 when entrainment is present. We also observe a local peak near 1.5 mm in Fig. 6(a), which might be due to different turbulence characteristics or microphysical responses. We will explore these aspects in future work.

The mean profile, together with the uncertainty in its estimation quantified using the standard error, indicates statistically significant enhancement of clustering under entrainment compared to the updraft case.

IV. DISCUSSIONS AND CONCLUDING REMARKS

Droplet clustering has been observed across various cloud regions, along with its prevalence near the cloud top [8,34,35,37]. The entrainment-mixing process near the cloud top suggests a potential coupling between entrainment-driven dynamics and droplet spatial organization. Previous studies have proposed that entrainment can modulate clustering [18,35], yet its understanding is limited due to the difficulty of performing collocated, high-spatiotemporal-resolution measurements of clustering and entrainment in field campaigns.

We investigated the role of cloud-top entrainment in modulating droplet clustering using collocated measurements of droplet spatial distributions and velocity vectors in the Pi cloud-convection chamber. The controlled laboratory setting enabled high spatiotemporal-resolution observations that are usually difficult to obtain in field experiments. A key outcome is the close correspondence between clustering characteristics observed in the chamber and those reported in field measurements [8,18,34], which suggests that key features of cloud droplet clustering can emerge independently of large-scale atmospheric variability and can be studied under well-defined initial and boundary conditions in cloud chambers. It allowed the role of entrainment to be examined more directly than is typically possible in the atmosphere, where multiple competing processes act simultaneously.

The bias-corrected RDF reveals the scale-dependent clustering of cloud droplets that peaks near the Kolmogorov scale and weakens at larger scales, a trend consistent with numerous field and laboratory studies [8,16,18,34]. However, differences might emerge due to variations in experimental configurations, environmental conditions, measurement techniques, and spatial dimensions. Specifically, we observe a sharp increase in clustering strength below the Kolmogorov scale, whereas Saw *et al.* [16] reported similar scale-change behavior at roughly 30 times the Kolmogorov scale. Furthermore, the observed clustering strength in our study is comparable to field observations [8,18,34], but it is relatively weak compared to certain laboratory findings [16].

We also observe intermittent behavior in clustering that is consistent with reported field observations [34]. Further, collocated velocity measurements reveal a positive relationship between clustering strength and entrainment intensity, indicating that entrainment can enhance localized clustering. Statistical analysis using the Kolmogorov-Smirnov test confirms that droplet-field nonuniformity increases during entrainment (downdraft) relative to no-entrainment (updraft) conditions.

Using a bias-mitigation strategy, we further show that two-dimensionally inferred measures of clustering strength [PCF(r)] during entrainment is estimated to be approximately twice that observed during updraft, and that this relative enhancement remains nearly constant beyond the Kolmogorov scale. A similar large-scale clustering due to scalar mixing has also been reported in wind-tunnel experiments [16]. Enhanced clustering can influence droplet-size broadening, collision-coalescence efficiency, and radiative transfer, all of which are critical to cloud evolution and precipitation formation. Observed modification of droplet spatial clustering by entrainment suggests that accounting for such effects in cloud-resolving and weather-prediction models may reduce uncertainties in representing cloud microphysics.

The present experiments have been conducted in a laboratory cloud with idealized and steady boundary conditions, which differ from the transient, multiscale, and radiatively influenced entrainment observed in atmospheric clouds. In addition, clustering and entrainment were analyzed in a two-dimensional plane, whereas real cloud processes occur in three dimensions. Hence, the estimated clustering, especially at small scales approaching the sheet thickness, can be different from their corresponding 3D system, altering the form of resulting RDF, including repressing or enhancing the magnitude of the signal [40,57]. Hence, the clustering signature explored in this work should be interpreted with caution when used to infer properties of the underlying 3D cloudy system.

The bias-mitigation strategy employed here is validated for the present configuration, but may need to be adapted for use with other experimental setups or observational geometries; however, the broader applicability of the bias-mitigation strategy is not limited to use in cloud physics. The bias-mitigation framework and clustering diagnostics developed here can be applied to other systems characterized by particle clustering in turbulent flows, such as atmospheric clouds, marine ecosystems with phytoplankton organization in upwelling and downwelling regions, and fuel-particle clustering in different combustion environments [2,4]. Future work should aim to extend these techniques to three dimensions and pursue coordinated field experiments with collocated measurements of entrainment and clustering. Such efforts can fully elucidate the role of entrainment in shaping droplet clustering and its consequences for cloud microphysics.

Here, clustering or relative clustering denotes any deviation from perfect randomness, i.e., departure from a random Poisson distribution at each resolved length scale in the system. Such nonrandomness may arise from clustering due to finite particle inertia [6], entrainment-induced clustering [16], or spatial inhomogeneities like voids. How the radial distribution function "responds" to various length-scales and strengths of clustering, such as can plausibly occur in turbulent clouds, has been explored in prior studies [14] using the analytic Matérn process (e.g., see Figs. 1 and 2 in that paper). More precise mapping of the RDF to specific geometric structures or inhomogeneities that may occur at cloud boundaries, such as in this experiment, represents an intriguing and fruitful direction for future research.

These results establish entrainment as a key modulator of droplet clustering at cloud top, primarily enhancing clustering at the inertial subrange. While the present study is based on idealized laboratory clouds, the findings underscore the need to account for entrainment-induced clustering in cloud-resolving and coarse-resolution models. Future work should extend these measurements to three dimensions and incorporate additional cloud-top processes to better assess the role of entrainment in atmospheric clouds.

ACKNOWLEDGMENTS

This work was supported by the US National Science Foundation (Grant No. AGS-2113060) and by the Simons Foundation (PD-Grant-01249402). Computational resources were provided by the MTU Superior Computing Facility.

DATA AVAILABILITY

Data supporting the findings can be obtained from Ref. [58].

APPENDIX A: BIAS-MITIGATION METHOD IN SCALE-DEPENDENT CLUSTERING

The RDF formally requires that the underlying system be spatially uniform (homogeneous) [59], yet this condition is rarely satisfied in real measurements, often due to systematic instrument biases or inherent inhomogeneity in the system. Despite this requirement, the radial distribution function has often been used when the underlying homogeneity is not certain. As the direct scale-localized measure of deviations from perfect spatial randomness, the RDF provides a measure of particle clustering that has many useful properties [32]. Further—although data may appear inhomogeneous, that does not mean that the data necessarily *are* inhomogeneous [60]. There is no unambiguous tool to definitively determine whether a real dataset is homogeneous, so RDF usage seems destined to persist even in circumstances where perhaps it should not [59].

If a system were to be statistically homogeneous but not *measured* to be statistically homogeneous due to instrumental imperfections and/or insensitivity, it is hoped that—with sufficient knowledge of the underlying instrumental measurement fidelity—the true underlying system RDF can still be estimated from measured data.

In recent work on *in situ* holographic cloud droplet measurements, an effort was made towards this goal with a new technique being introduced to determine whether or not clustering strength at any scale can unambiguously be considered large enough to be present even in the presence of instrumental sensitivity induced bias [8]. In the method used in that work, all droplets from an ensemble of consecutively measured and reconstructed hologram volumes are gathered into a single hologram, called a superhologram. Further, hologram sequences mimicking the measured data with their respective droplet counts are reconstructed from the droplet positions in the superhologram, but droplets are randomly assigned to different holograms in the sequence using 1000 random shuffles of position vectors of all droplets. Due to the

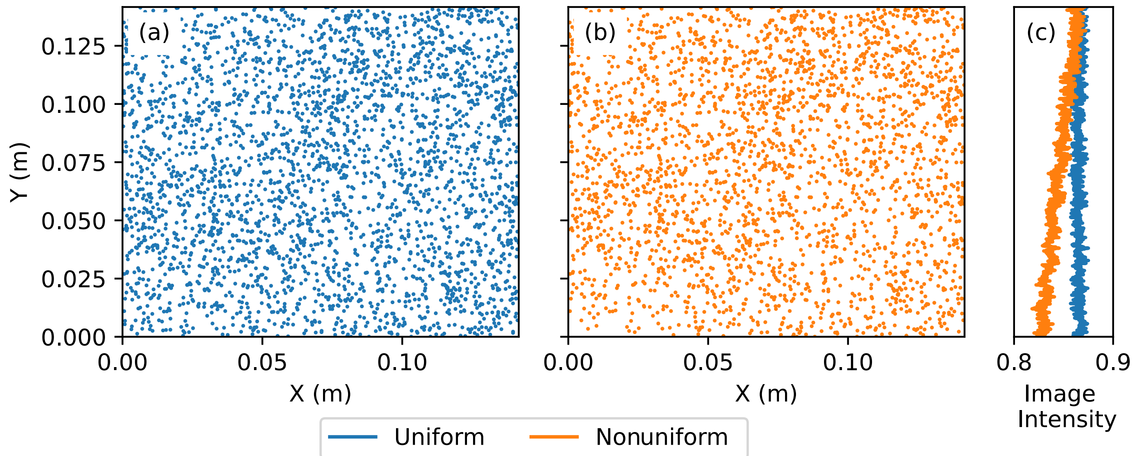

FIG. 7. Matérn distribution (a) spatially uniform, but locally clustered, (b) spatially nonuniform (due to added bias) but clustered, and (c) image intensity variation for panels (a) and (b).

random shuffling of detections among different holograms in the reconstructed simulated data, the reconstructed holograms lose all information about localized clustering but preserve systematic bias that existed throughout the duration of the measurement.

In the cited study, it was found that the measured RDF of the real data was outside of the envelope created by calculating the RDFs of the reconstructed and "homogenized" sequences, resulting in the conclusion that the measurements exhibited a spatial clustering signature that could not be attributed to instrumental biases alone.

In a recent study by Thiede *et al.* [34], the RDF from these systematic biases has been subtracted from the observed RDF to form a naive estimate of scale-dependent localized clustering amplitude. The authors of that study acknowledge that this correction is approximate and not rigorously valid unless certain (currently untestable) assumptions are made. Here, we adapt and expand this method under conditions when some reasonable assumptions about the measurement sensitivity profile are known.

The dominant bias in our recorded droplet fields is expected to arise from the diverging nature of the laser sheet, where the camera accurately detects a decreasing number of droplets in an image as we move away from the laser source. To mimic similar systematic bias in synthetic data, we can artificially thin a statistically homogeneous dataset by randomly removing droplets with a location-dependent probability. In particular, below we explore a homogeneous clustered system where we remove an increasing number of droplets from evenly divided ten vertical subareas of synthetic images, such that droplet counts decrease from top to bottom, which is clear from image intensity variation for uniform and nonuniform images [Fig. 7(c)]. A total of 15% of the droplets have been removed from the spatially uniform image to generate a nonuniform, biased one [Figs. 7 (a) and 7(b)].

To investigate the possible utility of a two-dimensional adaptation of the superhologram approach for estimating the true RDF from a deterministically biased collection of particles we generate 3600 test images using a Matérn process—a point process model that has a closed-form analytic expression for its radial distribution function and can be simply simulated in one, two, or threedimensions [33,46]. The Matérn point distribution was constructed within a unit square, with each distribution made from 300 parents, ten daughters per parent (λ_p), and a cluster radius of 0.1 unit (R); these three parameters are the free parameters that govern the construction of the distribution and its underlying radial distribution function [33,40].

The images were then rescaled to a 14 cm × 14 cm domain to keep the dimensions close to our observations. In this way, we constructed 3600 formally statistically homogeneous, although clustered, samples [e.g., Fig. 7(a)]. When we calculate the mean RDF ($g_h(r)$) using these images, we can accurately retrieve their clustering characteristics, in good agreement with theoretically calculated RDF ($g_{th}(r)$) using Eq. (A1), shown in Fig. 8.

The pair correlation function PCF(r) for such a two-dimensional Matérn process [40] is given by

$$g_{th}(r) - 1 = \mathrm{PCF}(r) = \begin{cases} 0, & \text{if } r > 2R, \\ \frac{2}{\pi^2 R^2 \lambda_p}\left[\arccos\left(\frac{r}{2R}\right) - \frac{r}{2R}\sqrt{1 - \frac{r^2}{4R^2}}\right], & \text{if } r < 2R, \end{cases} \tag{A1}$$

where λ_p is the mean number of droplets per parent and R is the radius of the circle surrounding each parent.

Using similar steps that have been used for the superhologram method [8], we calculate the superimage and corresponding RDF using the 3600 Matérn but thinned/biased images [Fig. 7(b)]. When we attempt to construct an estimate of $g_{\mathrm{th}}(r)$ by subtracting $g_s(r)$ from $g_t(r)$, we find that the resulting $g_c(r)$ (red curve in Fig. 8) overestimates the true theoretical RDF (dotted purple curve in Fig. 8). Evidently, random but inhomogeneous thinning is

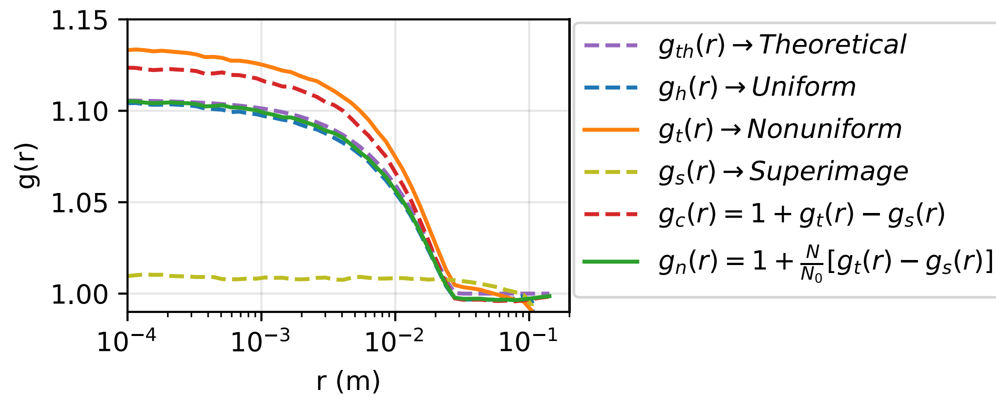

FIG. 8. Methods to mitigate systematic bias in RDF estimation and comparison with expected RDF. Test has been performed on the Matérn process.

not completely decoupled from RDF estimation in a trivial way.

Instead, we propose an alternative empirical correction scheme:

$$g_n(r) = 1 + \frac{N}{N_0}(g_t(r) - g_s(r)), \tag{A2}$$

where N is the number of detected drops in the inhomogeneously thinned image and N_0 is the number of drops that would have been detected in the underlying homogeneous, unthinned (but clustered) system. As the green curve very closely mimics the purple dotted curve in Fig. 8, this altered correction scheme appears to enable us to accurately retrieve the underlying physical RDF for this system under this measurement-induced inhomogeneity structure.

It appears that this empirical correction scheme works because in this system instrumental insensitivities or deterministic nonuniformities do not favor nor disfavor particle pairs at specific separation distances. Under these conditions, pair detections at all scales are expected to be diminished proportionally to the square of the ratio of the number densities between the actual nonuniform system and the underlying true homogeneous system. Hence, the average pair detections per observed particle scale linearly with this ratio which provides a basis for the plausibility of the N/N_0 scaling factor.

The above method appears to accurately enable retrieval of underlying scale-dependent clustering when N_0, background droplet counts in spatially uniform droplet fields, is known. Although N_0 can be accurately estimated by running a collocated droplet counter in experiments, such measurements are challenging and can also disturb the localized clustering behavior. Under circumstances when N_0 is not known but remains the same during two processes (like updraft and downdraft under the same thermal and microphysical forcing), this tool allows for a new way to estimate the relative strength of clustering without having to accurately measure the true system without bias. Consider two different processes, 1 and 2, under the same background forcings. $g_n(r)$ can be written using Eq. (A2) as

$$g_{n1}(r) - 1 = \frac{N_1}{N_0}(g_{t1}(r) - g_{s1}(r)), \tag{A3}$$

$$g_{n2}(r) - 1 = \frac{N_2}{N_0}(g_{t2}(r) - g_{s2}(r)). \tag{A4}$$

Division of Eq. (A3) by Eq. (A4) produces the relative strength of scale-dependent clustering, where we do not need to know N_0 [Eq. (A5)]. Although this does not provide information about absolute clustering, the quotient can be used to infer the relative strength, modulated by two distinct processes under the same background forcings:

$$\frac{g_{n1}(r) - 1}{g_{n2}(r) - 1} = \frac{N_1[g_{t1}(r) - g_{s1}(r)]}{N_2[g_{t2}(r) - g_{s2}(r)]}. \tag{A5}$$

We have tested the above technique on the Matérn process for three clustering strengths and two different levels of inhomogeneity (Table II). Note that in all cases, inhomogeneity has been added as described for Fig. 7(b). Cases 1 and 2 represent different clustering strengths, but they share the same systematic bias. Cases 1 and 3 correspond to different clustering strengths and systematic biases. Figure 9 shows that relative clustering, estimated using the above method for uniform and nonuniform droplet fields, is in good agreement with theoretically calculated ratios using Eq. (A1). This suggests that this method can be used to estimate the relative strength of localized clustering for downdraft (with entrainment) and updraft (no entrainment) for the same thermal and microphysical forcing using Eq. (A6)

$$\frac{g_\downarrow(r) - 1}{g_\uparrow(r) - 1} = \frac{N_\downarrow[g_{\downarrow,t}(r) - g_{\downarrow,s}(r)]}{N_\uparrow[g_{\uparrow,t}(r) - g_{\uparrow,s}(r)]}, \tag{A6}$$

where $\uparrow$ represents updraft and $\downarrow$ shows downdraft processes.

Note that the above analysis and testing have also been carried out using images with a Poisson distribution and varying degrees of vertical inhomogeneity (up to 20% droplets removal in maximum ten steps); the method satisfactorily produces the expected outcomes. For brevity, we have discussed

TABLE II. Parameters for Matérn process and added nonuniformity (bias) in terms of removed droplets (%), to test relative clustering.

Case	Cluster radius (unit)	Removed droplets (%)
1	0.1	15%
2	0.2	15%
3	0.15	20%

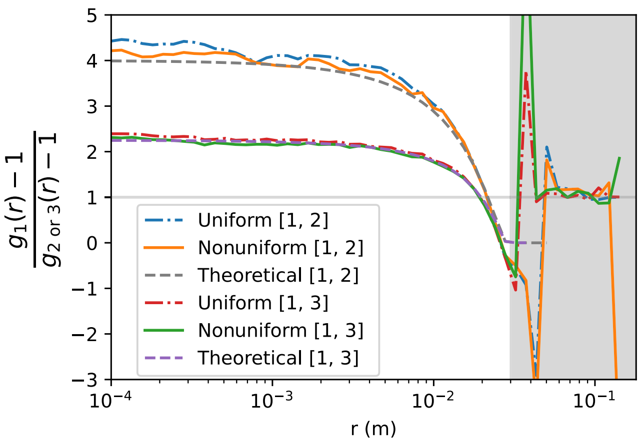

FIG. 9. Relative strength in scale-dependent clustering for spatially uniform and nonuniform droplet fields, and comparison with corresponding theoretical ratios. Cases 1 and 2 represent different clustering strengths but the same systematic bias, while Cases 1 and 3 correspond to different clustering strengths and different systematic biases.

one representative case. Note that although the above method seems to accurately mitigate biases in our observations, it must be tested for other types of biases, depending, e.g., upon experimental configurations and inhomogeneity geometries.

APPENDIX B: DERIVATION OF TURBULENCE KINETIC ENERGY DISSIPATION RATE

The general definition of the turbulence kinetic energy dissipation rate ε is written as

$$\varepsilon = 2\nu\langle s'_{ij}s'_{ij}\rangle, \tag{B1}$$

where $s'_{ij} = \frac{1}{2}(\frac{\partial u'_i}{\partial x_j} + \frac{\partial u'_j}{\partial x_i})$ is the fluctuating strain-rate tensor and ν is kinematic viscosity of the fluid. u'_i is the fluctuating velocity components that we get when mean velocities $(\bar{u}_i)$ are subtracted from instantaneous velocities (u_i) using Reynolds decomposition as follows:

$$u_i(x_j,t) = \bar{u}_i(x_j) + u'_i(x_j,t) \tag{B2}$$

and $\bar{u}_i(x_j)$ is time-averaged (or ensemble-averaged) flow field, calculated using

$$\bar{u}_i(x_j) = \frac{1}{N}\sum_{k=1}^{N} u_i(x_j,t_k), \tag{B3}$$

where N is total time steps.

Substituting $s'_{ij} = \frac{1}{2}(\frac{\partial u'_i}{\partial x_j} + \frac{\partial u'_j}{\partial x_i})$ into Eq. (B1),

$$\begin{aligned}\varepsilon &= 2\nu\left[\frac{1}{2}\left(\frac{\partial u'_i}{\partial x_j} + \frac{\partial u'_j}{\partial x_i}\right)\right]\left[\frac{1}{2}\left(\frac{\partial u'_i}{\partial x_j} + \frac{\partial u'_j}{\partial x_i}\right)\right]\\ &= \frac{1}{2}\nu\left(\frac{\partial u'_i}{\partial x_j} + \frac{\partial u'_j}{\partial x_i}\right)^2.\end{aligned} \tag{B4}$$

Expanding the squared binomial inside the summation for three component of velocities:

$$\varepsilon = \frac{1}{2}\nu\sum_{i=1}^{3}\sum_{j=1}^{3}\left[\left(\frac{\partial u'_i}{\partial x_j}\right)^2 + \left(\frac{\partial u'_j}{\partial x_i}\right)^2 + 2\left(\frac{\partial u'_i}{\partial x_j}\right)\left(\frac{\partial u'_j}{\partial x_i}\right)\right]. \tag{B5}$$

Further, $\sum(\frac{\partial u'_i}{\partial x_j})^2 = \sum(\frac{\partial u'_j}{\partial x_i})^2$, the above equation simplifies to

$$\varepsilon = \nu\sum_{i=1}^{3}\sum_{j=1}^{3}\left[\left(\frac{\partial u'_i}{\partial x_j}\right)^2 + \left(\frac{\partial u'_i}{\partial x_j}\right)\left(\frac{\partial u'_j}{\partial x_i}\right)\right]. \tag{B6}$$

Expanding into full expression and applying ensemble averaging:

$$\begin{aligned}\langle\varepsilon\rangle = \nu\Bigg[&2\left\langle\left(\frac{\partial u'}{\partial x}\right)^2\right\rangle + 2\left\langle\left(\frac{\partial v'}{\partial y}\right)^2\right\rangle + 2\left\langle\left(\frac{\partial w'}{\partial z}\right)^2\right\rangle\\ &+\left\langle\left(\frac{\partial u'}{\partial y}\right)^2\right\rangle + \left\langle\left(\frac{\partial u'}{\partial z}\right)^2\right\rangle + \left\langle\left(\frac{\partial v'}{\partial x}\right)^2\right\rangle\\ &+\left\langle\left(\frac{\partial v'}{\partial z}\right)^2\right\rangle + \left\langle\left(\frac{\partial w'}{\partial x}\right)^2\right\rangle + \left\langle\left(\frac{\partial w'}{\partial y}\right)^2\right\rangle\\ &+2\left\langle\frac{\partial u'}{\partial y}\frac{\partial v'}{\partial x}\right\rangle + 2\left\langle\frac{\partial u'}{\partial z}\frac{\partial w'}{\partial x}\right\rangle + 2\left\langle\frac{\partial v'}{\partial z}\frac{\partial w'}{\partial y}\right\rangle\Bigg].\end{aligned} \tag{B7}$$

To estimate the full 3D kinetic energy dissipation rate $\langle\varepsilon\rangle$ using only $u'(x,y)$ and $v'(x,y)$, physical and statistical assumptions are introduced to substitute for the missing out-of-plane terms [54]. These assumptions are

(1) Incompressibility ($\nabla\cdot\mathbf{u}' = 0$): The continuous fluid field satisfies continuity at all points:

$$\frac{\partial u'}{\partial x} + \frac{\partial v'}{\partial y} + \frac{\partial w'}{\partial z} = 0 \Rightarrow \frac{\partial w'}{\partial z} = -\left(\frac{\partial u'}{\partial x} + \frac{\partial v'}{\partial y}\right). \tag{B8}$$

This allows the unmeasured normal gradient variance $\langle(\frac{\partial w'}{\partial z})^2\rangle$ to be replaced with in-plane terms:

$$\left\langle\left(\frac{\partial w'}{\partial z}\right)^2\right\rangle = \left\langle\left(\frac{\partial u'}{\partial x}\right)^2\right\rangle + \left\langle\left(\frac{\partial v'}{\partial y}\right)^2\right\rangle + 2\left\langle\frac{\partial u'}{\partial x}\frac{\partial v'}{\partial y}\right\rangle. \tag{B9}$$

(2) Local isotropy: Small dissipation-scale turbulent eddies are assumed to have no preferred orientation. Considering transverse shear equality,

$$\left\langle\left(\frac{\partial u'}{\partial z}\right)^2\right\rangle = \left\langle\left(\frac{\partial u'}{\partial y}\right)^2\right\rangle,\quad \left\langle\left(\frac{\partial v'}{\partial z}\right)^2\right\rangle = \left\langle\left(\frac{\partial v'}{\partial x}\right)^2\right\rangle.$$

(3) Out-of-plane shear cross-correlations:

$$\left\langle\left(\frac{\partial w'}{\partial x}\right)^2\right\rangle = \left\langle\left(\frac{\partial v'}{\partial x}\right)^2\right\rangle,\quad \left\langle\left(\frac{\partial w'}{\partial y}\right)^2\right\rangle = \left\langle\left(\frac{\partial u'}{\partial y}\right)^2\right\rangle.$$

(4) Unmeasured cross-derivative cancellation:

$$\left\langle\frac{\partial u'}{\partial z}\frac{\partial w'}{\partial x}\right\rangle = \left\langle\frac{\partial u'}{\partial y}\frac{\partial v'}{\partial x}\right\rangle,\quad \left\langle\frac{\partial v'}{\partial z}\frac{\partial w'}{\partial y}\right\rangle = \left\langle\frac{\partial u'}{\partial y}\frac{\partial v'}{\partial x}\right\rangle.$$

(5) Homogeneity: Boundary and edge effects at small viscous scales do not introduce directional bias.

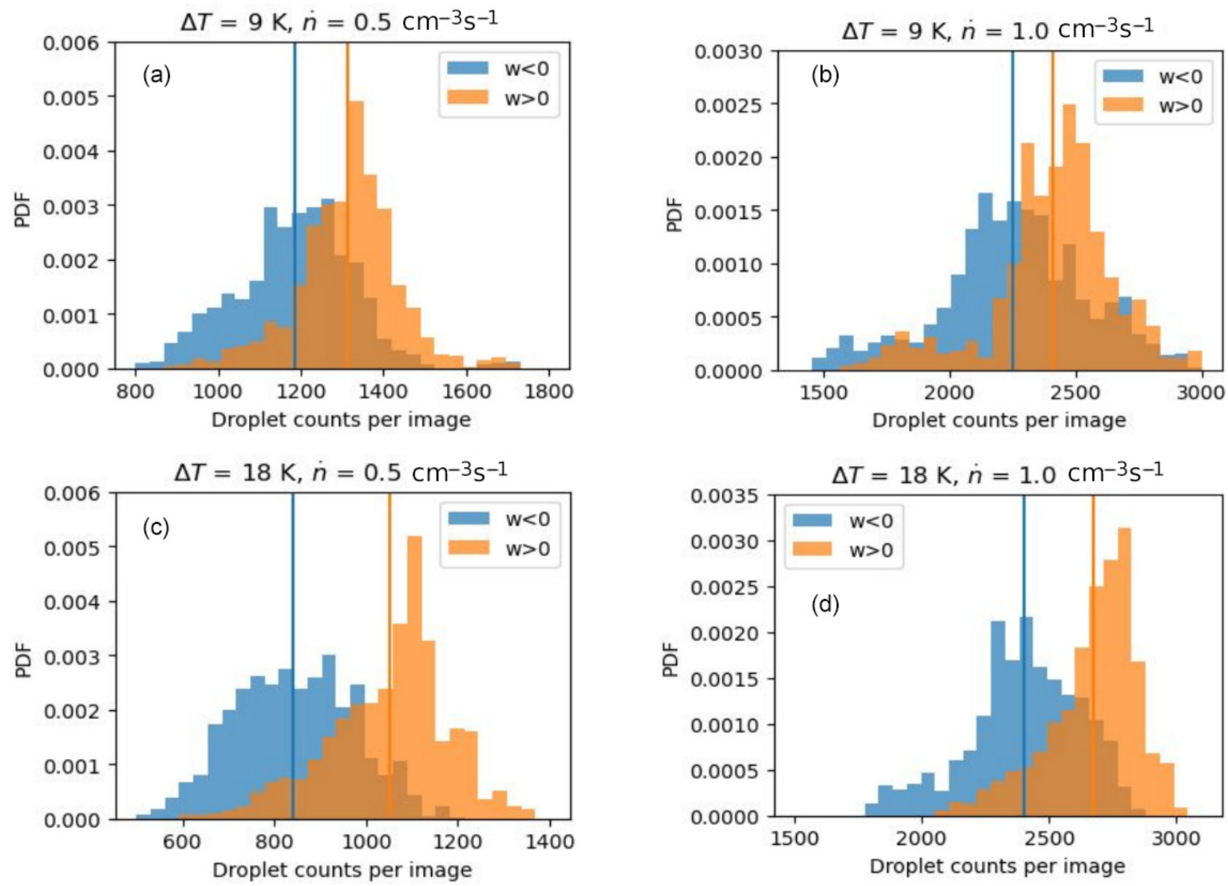

FIG. 10. PDFs of droplet counts per image for all experimental conditions, conditioned on whether the vertical velocity is downward (entrainment) or upward (no entrainment). The blue vertical line shows the mean droplet count for entrainment conditions, whereas the orange vertical line indicates the mean droplet count for no-entrainment conditions.

By replacing all eight out-of-plane terms with their in-plane isotropic equivalents into Eq. (B7), PIV-derived velocity field can be used to estimate ε as

$$\langle\varepsilon\rangle_{\text{2D-PIV}} = \nu\Bigg[4\Bigg\langle\left(\frac{\partial u'}{\partial x}\right)^2\Bigg\rangle + 4\Bigg\langle\left(\frac{\partial v'}{\partial y}\right)^2\Bigg\rangle + 2\Bigg\langle\left(\frac{\partial u'}{\partial y}\right)^2\Bigg\rangle + 2\Bigg\langle\left(\frac{\partial v'}{\partial x}\right)^2\Bigg\rangle + 2\Bigg\langle\frac{\partial u'}{\partial y}\frac{\partial v'}{\partial x}\Bigg\rangle\Bigg]. \tag{B10}$$

Equation (B10) has been used to calculate the dissipation rate. Furthermore, the calculated values of ε were validated against the dissipation equation proposed by Gomes-Fernandes *et al.* [54].

APPENDIX C: DROPLET DEPLETION DURING ENTRAINMENT

The PDFs of droplet counts per image for all experimental conditions, conditioned on whether the vertical velocity is downward (entrainment) or upward (no entrainment), are shown in Fig. 10. It shows that entrainment leads to the depletion of cloud droplets, indicating localized inhomogeneous mixing [42].

APPENDIX D: SNAPSHOTS OF 2D DROPLET FIELD UNDER WEAK AND STRONG CLUSTERING

2D snapshots of cloud-droplet fields under weak and strong clustering for two different cases ($\Delta T = 9$ K, $\dot{n} = 0.5$ cm^{-3} s^{-1}; $\Delta T = 18$ K, $\dot{n} = 1.0$ cm^{-3} s^{-1}) are shown in Figs. 11 and 12, respectively.

APPENDIX E: SCATTER PLOT FOR DIFFERENT VARIABLES

Figure 13 shows the scatter plots used to analyze correlations between the various variables. Although it is evident that not all variables accurately satisfy the assumptions required for a Pearson correlation analysis, we applied it uniformly across all variables to maintain consistency and to evaluate their first-order dependencies.

APPENDIX F: ERROR ANALYSIS FOR RELATIVE STRENGTH OF CLUSTERING

Apart from systematic instrument bias, there is inherent uncertainty in the analysis due to pixelation errors, limited sample areas, and sample variability. It can be significant when multiple mathematical operations are involved

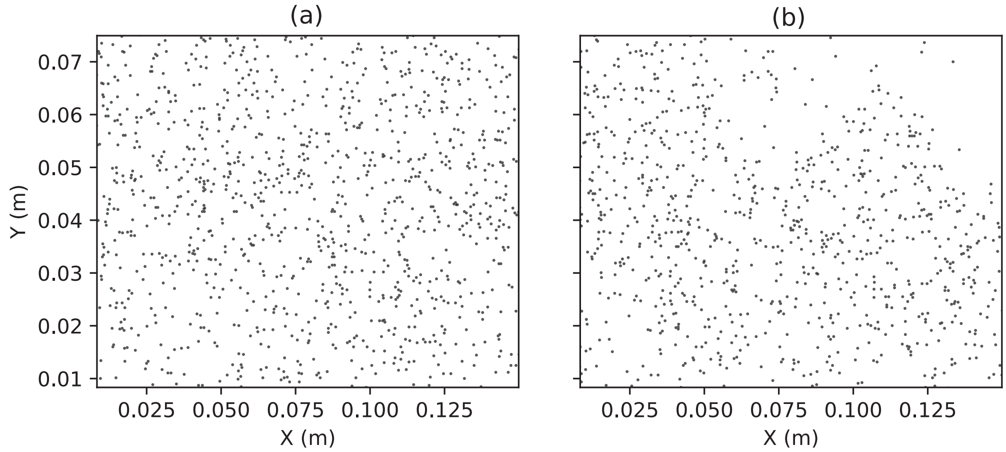

FIG. 11. 2D snapshots of cloud-droplet fields under weak and strong clustering for $\Delta T = 9$ K, $\dot{n} = 0.5$ cm^{-3} s^{-1}, (a) weak clustering and (b) Strong clustering.

on the observed dataset [61]. Hence, to quantify uncertainty in the relative strength of clustering between downdraft (entrainment) and updraft (no entrainment), mean, standard deviation, and standard error are estimated as follows. Note that standard deviation represents sample-to-sample uncertainty, while standard error indicates uncertainty in estimating mean clustering [61]. After excluding images based on invalid velocity vectors, 7200 images in ten equal chunks have been considered for the entrainment as well as no-entrainment cases for all experimental conditions. To account for pixelation errors, the position of each droplet was jittered uniformly between ±0.5 pixels (probable error due to pixelation), and corresponding $g_t(r)$ and $g_s(r)$ were calculated.

First, we calculate median RDFs over 50 jittered ensemble members and take chunkwise mean on $g_t(r)$ and $g_s(r)$. The denominator and numerator of the right side of Eq. (A6) are independently calculated, which have been used to estimate the mean denominator and numerator, and their corresponding standard deviation and standard error. Further, the mean denominator and numerator are divided to obtain the mean scale-dependent clustering, and their standard deviation and error are estimated using the rule of error propagation for division [61].

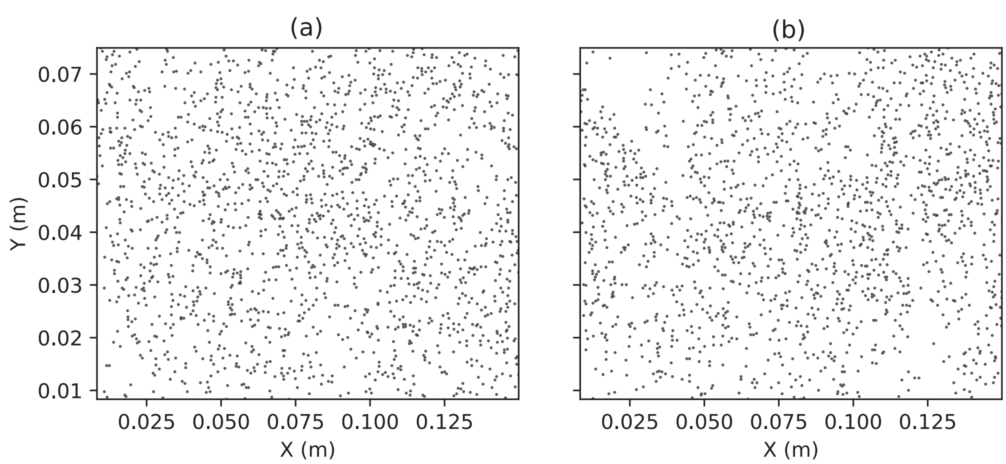

FIG. 12. 2D snapshots of cloud-droplet fields under weak and strong clustering for $\Delta T = 18$ K, $\dot{n} = 1.0$ cm^{-3} s^{-1}, (a) weak clustering and (b) Strong clustering.

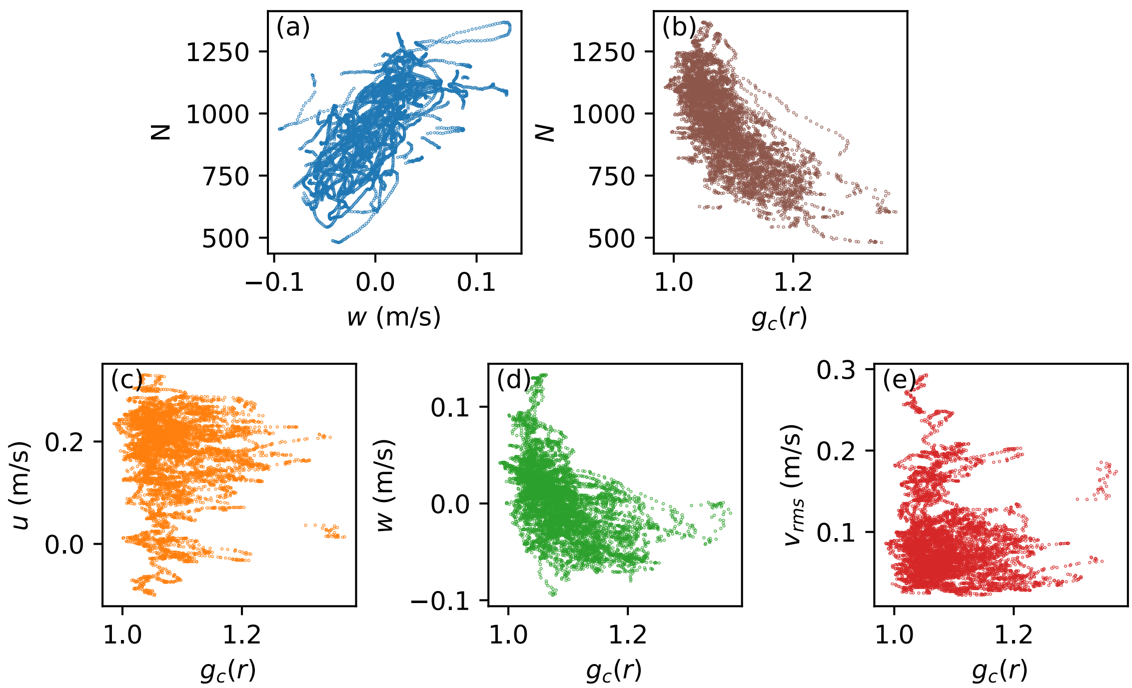

FIG. 13. Scatter plot between different variables for strongly forced clouds ($\Delta T = 18\,\mathrm{K}$, $\dot{n} = 0.5\,\mathrm{cm}^{-3}\,\mathrm{s}^{-1}$): (a) vertical velocity (w) and droplet counts per image (N), (b) corrected RDF ($g_c(r)$) and N, (c) $g_c(r)$ and horizontal velocity (u), (d) $g_c(r)$ and vertical velocity (w), and (e) $g_c(r)$ and root-mean-square velocity (v_{rms}). Note that $g_c(r)$ has been calculated at $r = 0.001$ m.

[1] L. Pan, P. Padoan, J. Scalo, A. G. Kritsuk, and M. L. Norman, Turbulent clustering of protoplanetary dust and planetesimal formation, Astrophys. J. **740**, 6 (2011).

[2] M. Borgnino, J. Arrieta, G. Boffetta, F. De Lillo, and I. Tuval, Turbulence induces clustering and segregation of non-motile, buoyancy-regulating phytoplankton, J. R. Soc. Interface **16**, 20190324 (2019).

[3] F. Azam and F. Malfatti, Microbial structuring of marine ecosystems, Nat. Rev. Microbiol. **5**, 782 (2007).

[4] L. Schmidt, I. Fouxon, and M. Holzner, Inertial particles distribute in turbulence as Poissonian points with random intensity inducing clustering and supervoiding, Phys. Rev. Fluids **2**, 074302 (2017).

[5] J. Krüger, N. E. Haugen, D. Mitra, and T. Løvås, The effect of turbulent clustering on particle reactivity, Proc. Combust. Inst. **36**, 2333 (2017).

[6] A. B. Kostinski and R. A. Shaw, Scale-dependent droplet clustering in turbulent clouds, J. Fluid Mech. **434**, 389 (2001).

[7] H. R. Pruppacher and J. D. Klett, *Microphysics of Clouds and Precipitation: Reprinted 1980* (Springer Science & Business Media, Dordrecht, Netherlands, 2012).

[8] M. L. Larsen, R. A. Shaw, A. B. Kostinski, and S. Glienke, Fine-scale droplet clustering in atmospheric clouds: 3D radial distribution function from airborne digital holography, Phys. Rev. Lett. **121**, 204501 (2018).

[9] R. Srivastava, Growth of cloud drops by condensation: A criticism of currently accepted theory and a new approach, J. Atmos. Sci. **46**, 869 (1989).

[10] W. W. Grabowski and L.-P. Wang, Growth of cloud droplets in a turbulent environment, Annu. Rev. Fluid Mech. **45**, 293 (2013).

[11] A. B. Kostinski, On the extinction of radiation by a homogeneous but spatially correlated random medium, J. Opt. Soc. Am. A **18**, 1929 (2001).

[12] R. A. Shaw, A. B. Kostinski, and D. D. Lanterman, Super-exponential extinction of radiation in a negatively correlated random medium, J. Quant. Spectrosc. Radiat. Transfer **75**, 13 (2002).

[13] M. L. Larsen and A. S. Clark, On the link between particle size and deviations from the Beer–Lambert–Bouguer law for direct transmission, J. Quant. Spectrosc. Radiat. Transfer **133**, 646 (2014).

[14] C. D. Packard, M. L. Larsen, W. H. Cantrell, and R. A. Shaw, Light scattering in a spatially-correlated particle field: Role of the radial distribution function, J. Quant. Spectrosc. Radiat. Transfer **236**, 106601 (2019).

[15] H. Siebert, S. Gerashchenko, A. Gylfason, K. Lehmann, L. Collins, R. Shaw, and Z. Warhaft, Towards understanding the role of turbulence on droplets in clouds: *In situ* and laboratory measurements, Atmos. Res. **97**, 426 (2010).

[16] E.-W. Saw, R. A. Shaw, J. P. Salazar, and L. R. Collins, Spatial clustering of polydisperse inertial particles in turbulence: II. Comparing simulation with experiment, New J. Phys. **14**, 105031 (2012).

[17] K. Matsuda, R. Onishi, M. Hirahara, R. Kurose, K. Takahashi, and S. Komori, Influence of microscale turbulent droplet clustering on radar cloud observations, J. Atmos. Sci. **71**, 3569 (2014).

[18] S. Glienke, A. B. Kostinski, R. A. Shaw, M. L. Larsen, J. P. Fugal, O. Schlenczek, and S. Borrmann, Holographic observations of centimeter-scale nonuniformities within marine stratocumulus clouds, J. Atmos. Sci. **77**, 499 (2020).

[19] S. K. Krueger, C.-W. Su, and P. A. McMurtry, Modeling entrainment and finescale mixing in cumulus clouds, J. Atmos. Sci. **54**, 2697 (1997).

[20] A. Cimarelli and G. Boga, Numerical experiments on turbulent entrainment and mixing of scalars, J. Fluid Mech. **927**, A34 (2021).

[21] F. Yang, Y. M. Sua, Z. Zheng, J. Anderson, H. F. Sadi, J. M. Yeom, S. P. Singh, P. Hou, W. H. Cantrell, E. R. Lewis, *et al.*, High-resolution lidar observations of sedimentation-induced size sorting of droplets near a laboratory cloud top, Proc. Natl. Acad. Sci. USA **122**, e2505421122 (2025).

[22] R. Paoli and K. Shariff, Turbulent condensation of droplets: Direct simulation and a stochastic model, J. Atmos. Sci. **66**, 723 (2009).

[23] K. D. Squires and J. K. Eaton, Preferential concentration of particles by turbulence, Phys. Fluids **3**, 1169 (1991).

[24] M. Obligado, T. Teitelbaum, A. Cartellier, P. Mininni, and M. Bourgoin, Preferential concentration of heavy particles in turbulence, J. Turbul. **15**, 293 (2014).

[25] J. Chun, D. L. Koch, S. L. Rani, A. Ahluwalia, and L. R. Collins, Clustering of aerosol particles in isotropic turbulence, J. Fluid Mech. **536**, 219 (2005).

[26] K. Lehmann, H. Siebert, M. Wendisch, and R. A. Shaw, Evidence for inertial droplet clustering in weakly turbulent clouds, Tellus B: Chem. Phys. Meteorol. **59**, 57 (2007).

[27] O. Ayala, B. Rosa, L.-P. Wang, and W. W. Grabowski, Effects of turbulence on the geometric collision rate of sedimenting droplets. Part 1. Results from direct numerical simulation, New J. Phys. **10**, 075015 (2008).

[28] E.-W. Saw, J. P. Salazar, L. R. Collins, and R. A. Shaw, Spatial clustering of polydisperse inertial particles in turbulence: I. Comparing simulation with theory, New J. Phys. **14**, 105030 (2012).

[29] R. A. Shaw, Particle-turbulence interactions in atmospheric clouds, Annu. Rev. Fluid Mech. **35**, 183 (2003).

[30] S. Thomas, M. Ovchinnikov, F. Yang, D. van der Voort, W. Cantrell, S. K. Krueger, and R. A. Shaw, Scaling of an atmospheric model to simulate turbulence and cloud microphysics in the Pi chamber, J. Adv. Model. Earth Syst. **11**, 1981 (2019).

[31] E. W. Saw, R. A. Shaw, S. Ayyalasomayajula, P. Y. Chuang, and A. Gylfason, Inertial clustering of particles in high-Reynolds-number turbulence, Phys. Rev. Lett. **100**, 214501 (2008).

[32] R. A. Shaw, A. B. Kostinski, and M. L. Larsen, Towards quantifying droplet clustering in clouds, Q. J. R. Meteorol. Soc. **128**, 1043 (2002).

[33] M. L. Larsen and R. A. Shaw, A method for computing the three-dimensional radial distribution function of cloud particles from holographic images, Atmos. Meas. Tech. **11**, 4261 (2018).

[34] B. Thiede, M. L. Larsen, F. Nordsiek, O. Schlenczek, Y. Kim, E. Bodenschatz, and G. Bagheri, Highly localized droplet clustering in shallow cumulus clouds, Proc. Natl. Acad. Sci. USA **123**, e2602976123 (2026).

[35] J. J. D'Alessandro and G. M. McFarquhar, Impacts of drop clustering and entrainment-mixing on mixed phase shallow cloud properties over the Southern Ocean: Results from SOCRATES, J. Geophys. Res.: Atmos. **128**, e2023JD038622 (2023).

[36] Y. Liu, J. Yang, G. Zhao, Y. Deng, C. Lu, Y. Yin, X. Jing, and Y. Wang, On the scale of particle clustering induced by inhomogeneous entrainment-mixing in mixed-phase cumulus clouds, Geophys. Res. Lett. **51**, e2023GL107645 (2024).

[37] J. J. D'Alessandro, R. Wood, and P. N. Blossey, Drop clustering and drop size correlations from holographic imagery suggest cloud droplet spectral broadening via entrainment-mixing, Atmos. Chem. Phys. **26**, 4067 (2026).

[38] K. Chang, J. Bench, M. Brege, W. Cantrell, K. Chandrakar, D. Ciochetto, C. Mazzoleni, L. Mazzoleni, D. Niedermeier, and R. Shaw, A laboratory facility to study gas–aerosol–cloud interactions in a turbulent environment: The π chamber, Bull. Am. Meteorol. Soc. **97**, 2343 (2016).

[39] P. J. Ireland, A. D. Bragg, and L. R. Collins, The effect of Reynolds number on inertial particle dynamics in isotropic turbulence. Part 2. Simulations with gravitational effects, J. Fluid Mech. **796**, 659 (2016).

[40] M. L. Larsen, C. A. Briner, and P. Boehner, On the recovery of 3D spatial statistics of particles from 1D measurements: Implications for airborne instruments, J. Atmos. Ocean. Technol. **31**, 2078 (2014).

[41] J. M. Yeom, H. Fahandezh Sadi, J. C. Anderson, F. Yang, W. Cantrell, and R. A. Shaw, Cloud microphysical response to entrainment of dry air containing aerosols, npj Clim. Atmos. Sci. **8**, 8 (2025).

[42] J. M. Yeom, I. Helman, P. Prabhakaran, J. C. Anderson, F. Yang, R. A. Shaw, and W. Cantrell, Cloud microphysical response to entrainment and mixing is locally inhomogeneous and globally homogeneous: Evidence from the lab, Proc. Natl. Acad. Sci. USA **120**, e2307354120 (2023).

[43] A. Sofi, M. Shah, and K. Asokan, Structural, optical and electrical properties of ITO thin films, J. Electron. Mater. **47**, 1344 (2018).

[44] G. Bradski and K. Adrian, *Learning OpenCV: Computer vision with the OpenCV library* (O'Reilly Media, Inc., California, USA, 2008).

[45] A. Liberzon, D. Lasagna, M. Aubert, P. Bachant, E. Mahmoodtabar, T. Käufer, Jakirkham, A. Bauer, B. Vodenicharski, C. Dallas, E. Yang, J. Borg, M. M. Farzan, Tomerast, and Ranleu, OpenPIV-Python, Version 0.23.3, Zenodo, 2020, https://doi.org/10.5281/zenodo.4320056.

[46] S. N. Chiu, D. Stoyan, W. S. Kendall, and J. Mecke, *Stochastic Geometry and its Applications* (John Wiley & Sons, Chichester, UK, 2013).

[47] F. J. Massey, Jr., The Kolmogorov-Smirnov test for goodness of fit, J. Am. Stat. Assoc. **46**, 68 (1951).

[48] J. G. Skellam, The frequency distribution of the difference between two Poisson variates belonging to different populations, J. R. Stat. Soc. **109**, 296 (1946).

[49] H. Fahandezh Sadi, E. R. Lewis, K. F. Gali, F. Yang, J. C. Anderson, S. P. Singh, J. M. Yeom, W. Cantrell, and R. A. Shaw, Large aerosol particles favor haze conditions through limitations on water budget and activation kinetics, Geophys. Res. Lett. **53**, e2025GL117310 (2026).

[50] T. MacMillan, R. A. Shaw, W. H. Cantrell, and D. H. Richter, Direct numerical simulation of turbulence and microphysics in the Pi chamber, Phys. Rev. Fluids **7**, 020501 (2022).

[51] S. Thomas, F. Yang, M. Ovchinnikov, W. Cantrell, and R. A. Shaw, Scaling of turbulence and microphysics in a convection–

cloud chamber of varying height, J. Adv. Model. Earth Syst. **15**, e2022MS003304 (2023).

[52] J. C. Anderson, S. Thomas, P. Prabhakaran, R. A. Shaw, and W. Cantrell, Effects of the large-scale circulation on temperature and water vapor distributions in the π chamber, Atmos. Meas. Tech. Discuss. **14**, 5473 (2021).

[53] S. B. Pope, Turbulent flows, Meas. Sci. Technol. **12**, 2020 (2001).

[54] R. Gomes-Fernandes, B. Ganapathisubramani, and J. Vassilicos, Particle image velocimetry study of fractal-generated turbulence, J. Fluid Mech. **711**, 306 (2012).

[55] D. Xu and J. Chen, Accurate estimate of turbulent dissipation rate using PIV data, Exp. Therm. Fluid Sci. **44**, 662 (2013).

[56] M. A. Yavuz, R. P. J. Kunnen, G. J. F. Van Heijst, and H. J. H. Clercx, Extreme small-scale clustering of droplets in turbulence driven by hydrodynamic interactions, Phys. Rev. Lett. **120**, 244504 (2018).

[57] G. L. Holtzer and L. R. Collins, Relationship between the intrinsic radial distribution function for an isotropic field of particles and lower-dimensional measurements, J. Fluid Mech. **459**, 93 (2002).

[58] S. P. Singh, M. Larsen, J. Anderson, H. F. Sadi, J. Yeom, W. Cantrell, and R. A. Shaw, Droplet clustering signatures of entrainment in clouds, 2026, Retrieved from: https://digitalcommons.mtu.edu/all-datasets/81.

[59] M. L. Larsen, Scale localization of cloud particle clustering statistics, J. Atmos. Sci. **69**, 3277 (2012).

[60] C. Wunsch, The interpretation of short climate records, with comments on the North Atlantic and Southern Oscillations, Bull. Am. Meteorol. Soc. **80**, 245 (1999).

[61] J. R. Taylor, *An Introduction to Error Analysis: The Study of Uncertainties in Physical Measurements* (MIT Press, New York, USA, 2022).